

Comparison of negative refractive index materials with circular, elliptical and rectangular holes

Zahyun Ku and S. R. J. Brueck

Center for High Technology Materials and Department of Electrical and Computer Engineering,
University of New Mexico, Albuquerque, NM 87106, USA
brueck@chtm.unm.edu

Abstract: Negative-index metamaterials (NIMs) at near infrared wavelengths ($\sim 2 \mu\text{m}$) are fabricated with circular, elliptical and rectangular holes penetrating through metal/dielectric/metal films. All three NIM structures exhibit similar figures of merit; however, the transmission is higher for the NIM with rectangular holes as a result of an improved impedance match with the substrate-superstrate (air-glass) combination.

©2007 Optical Society of America

OCIS codes: (160.4760) Optical properties; (160.4670) Optical materials; (260.5740) Resonance; (310.6860) Thin films, optical properties.

References and links

1. D. R. Smith, W. J. Padilla, D. C. Vier, S. C. Nemat-Nasser, and S. Schultz, "Composite medium with simultaneously negative permeability and permittivity," *Phys. Rev. Lett.* **84**, 4184-4187 (2000).
2. R. A. Shelby, D. R. Smith, and S. Schultz, "Experimental verification of a negative index of refraction," *Science* **292**, 77-79 (2002).
3. V. G. Veselago, "The electrodynamics of substances with simultaneously negative values of ϵ and μ ," *Sov. Phys. USPEKHI*, **10** 509 (1968).
4. J. B. Pendry, "Negative refraction makes a perfect lens," *Phys. Rev. Lett.* **85**, 3966-3969 (2000).
5. S. O'Brien and J. B. Pendry, "Magnetic activity at infrared frequencies in structured metallic photonic crystals," *J. Phys. Condens. Matter* **14**, 6383-6394 (2002).
6. N.-C. Panoui and R. M. Osgood, "Influence of the dispersive properties of metals on the transmission characteristics of left-handed materials," *Phys. Rev. E* **68**, 016611(2003).
7. N.-C. Panoui and R. M. Osgood, "Numerical investigation of negative refractive index metamaterials at infrared and optical frequencies," *Opt. Commun.* **233**, 331-337 (2003).
8. S. Zhang, W. Fan, A. Frauenglass, B. Minhas, K. J. Malloy and S. R. J. Brueck, "Demonstration of Mid-Infrared Resonant Magnetic Nanostructures exhibiting a negative permeability," *Phys. Rev. Lett.* **94**, 037402 (2005).
9. T. J. Yen, W. J. Padilla, N. Fang, D. C. Vier, D. R. Smith, J. B. Pendry, D. N. Basov, and X. Zhang, "Terahertz magnetic response from artificial materials," *Science* **303**, 1494-1496 (2004).
10. N. Katsarakis, G. Konstantinidis, A. Kostopoulos, R. S. Penciu, T. F. Gundogdu, Th Koschny, M. Kafesaki, E. N. Economou and C. M. Soukoulis "Magnetic response of split-ring resonators in the far infrared frequency regime," *Opt. Lett.* **30**, 1348-1350 (2005).
11. S. Linden, C. Enkrich, M. Wegener, J. Zhou, T. Koschny, and C. M. Soukoulis, "Magnetic response of metamaterials at 100 Terahertz," *Science* **306**, 1351-1353 (2004).
12. C. Enkrich, F. Pérez-Willard, D. Gerthsen, J. F. Zhou, T. Koschny, C. M. Soukoulis, M. Wegener and S. Linden "Focused-ion-beam nanofabrication of near-infrared magnetic metamaterials," *Adv. Mat.* **17**, 2547-2549 (2005).
13. S. Zhang, W. Fan, N. C. Panoui, K. J. Malloy, R. M. Osgood and S. R. J. Brueck, "Experimental demonstration of near-infrared negative-index metamaterials," *Phys. Rev. Lett.* **95**, 137404 (2005).
14. V. M. Shalaev, W. Cai, U. K. Chettiar, H-K. Yuan, A. K. Sarychev, V. P. Drachev and A. V. Kildishev, "Negative index of refraction in optical metamaterials," *Opt. Lett.* **30**, 3356-3358 (2005).
15. S. Zhang, W. Fan, K. J. Malloy, S. R. J. Brueck, N.-C. Panoui and R. M. Osgood, "Near-infrared double negative metamaterials," *Opt. Express* **13**, 4922-4930 (2005).
16. S. Zhang, W. Fan, K. J. Malloy, S. R. J. Brueck, N.-C. Panoui and R. M. Osgood, "Demonstration of metal-dielectric negative-index metamaterials with improved performance at optical frequencies," *J. Opt. Soc. Am. B* **23**, 434-438 (2006).

17. G. Dolling, C. Enkrich, W. Wegener, C.M. Soukoulis and S. Linden, "Low-loss negative-index metamaterial at telecommunication wavelengths," *Opt. Lett.* **31**, 1800-1802 (2006)
 18. S. R. J. Brueck, "Optical and Interferometric Lithography – Nanotechnology Enablers," *Proc. IEEE* **93**, 1704-1721 (2005).
 19. M. G. Moharam and T.K. Gaylord, "Rigorous coupled-wave analysis of planar-grating diffraction," *J. Opt. Soc. Am.* **71**, 811-818 (1981).
 20. B. K. Minhas, W. Fan, K. Agi, S. R. J. Brueck and K. J. Malloy, "Metallic inductive and capacitive grids: theory and experiment," *J. Opt. Soc. Am. A* **19**, 1352-1359 (2002).
 21. M. A. Ordal, L. L. Long, R. J. Bell, S. E. Bell, R. R. Bell, R.W. Alexander, and C. A. Ward, "Optical properties of the metals Al, Co, Cu, Au, Fe, Pb, Ni, Pd, Pt, Ag, Ti and W in the infrared and far infrared," *Appl. Opt.* **22**, 1099 (1983).
 22. D. R. Smith and S. Schultz, "Determination of effective permittivity and permeability of metamaterials from reflection and transmission coefficients," *Phys. Rev.* **B 65**, 195104. (2002).
-

1. Introduction

The initial demonstrations of negative index metamaterials (NIMs) [1, 2] along with theoretical predictions of potential applications such as imaging beyond the diffraction limit [3,4] have led to intense interest in extending these results to shorter near-infrared and visible wavelengths. Over the past few years, there have been theoretical efforts towards the realization of short wavelength magnetic metamaterials [5] and NIMs [6, 7], and experimental demonstration of magnetic metamaterials at far-, mid-, near-infrared and visible wavelengths [8-12] and near-infrared NIMs [13, 14].

Recently, Zhang *et al.* proposed [13] and demonstrated [15] a NIM structure composed of two parts: the negative electric permittivity (ϵ) results from an array of thin metal wires parallel to the direction of electric field and the negative magnetic permeability (μ) from a pair of finite-width metal stripes separated by a dielectric layer along the direction of the incident magnetic field. The resulting structure is a 2D array of holes penetrating completely through a metal-dielectric-metal film stack. In the initial experiments, circular holes were used, which led to relatively wide metal stripes contributing to the permittivity, to a large negative ϵ , and a significant impedance mismatch between the metamaterial and the incident and transmitted media. The structure was metal-like and most of the incident energy was reflected, with only ~5% transmission in the negative-index spectral region. The experimental figure of merit [FOM $\equiv -\text{Re}(n)/\text{Im}(n)$] was only about 0.5 for this structure. This result was improved using elliptical apertures with narrower metal stripes parallel to the electric field, with about 20% transmission and a FOM of ~ 0.9 [16]. Dolling *et al.* [17] introduced a variant with rectangular apertures (the fishnet structure) and achieved both a higher transmission (~ 65%) and an improved FOM (~ 3) and argued that the improvement was due to the improved material properties (Ag vs. Au) and to the square structure which provided a constant width across the aperture in contrast to the varying chord of the elliptical structure. However, their experiment used a different material system (Ag-MgF₂-Ag in place of Au-Al₂O₃-Au) and was resonant at a different wavelength (1.5 μm instead of 2 μm) making a detailed understanding of the structural impact on the metamaterial properties difficult. In this work we fabricate, in the Au-Al₂O₃-Au material system, a series of three structures with 2D arrays of circular, elliptical and rectangular apertures resonant at similar wavelengths to allow a direct comparison of the metamaterial properties. We find that the impact of the geometry of the individual apertures is most dramatic on the impedance and that there is only a weak dependence of the FOM on the aperture geometry.

2. Design and fabrication

The sample structure consists of a glass substrate with a pair of metallic films (30-nm thick layers of Au) separated by a dielectric film (60-nm thick layer of Al₂O₃), with a 2-dimensional (2D) square periodic array of circular, elliptical and rectangular holes penetrating through the multilayer structure. Schematic representations of these structures are shown in Fig. 1.

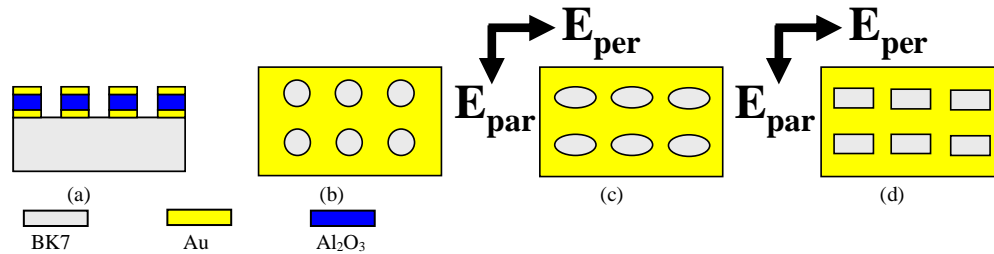


Fig. 1. Schematic views of metamaterial structures with circular, elliptical and rectangular holes. (a) Side view of metal-dielectric-metal film stack. Top view of NIMs with (b) circular (c) elliptical (d) rectangular holes. In (c) and (d), the polarization can be directed along either the major (long) or the minor (short) axis, which are denoted E_{par} (electric field parallel to the minor/short axis) and E_{per} (electric field perpendicular to the minor/short axis) polarization, respectively.

The procedure for fabricating the circular and elliptical holes through the multilayer is as follows. A thick layer of a bottom-antireflection-coating polymer (BARC) was spun onto a BK7 glass substrate, followed by a layer of negative I-line photoresist (NR7-500P). Interferometric lithography (IL), using two coherent UV laser beams (3rd harmonic of a YAG laser at $\lambda=355$ nm) was used to define a 2D array of circular or elliptical holes in the PR layer. The pitch of 823 nm, controlled by the angle between two UV beams, was fixed for all results reported here. IL was used to fabricate large-area (2.5×2.5 cm²), uniform samples, making sample characterization convenient [18]. In order to define a 2D array of circular (elliptical) holes in PR layer, we performed two successive 1D exposures in orthogonal directions with the same (different) doses. After exposure and development, a 2D array of circular (elliptical) holes was formed with a diameter of 400 nm (534 nm, 340 nm in major and minor axis, respectively) in the PR layer. Next an e-beam metal evaporation was used to deposit a thin film of Ti atop the PR layer, followed by a lift-off process using acetone to remove the PR. This resulted in an array of circular (elliptical) Ti disks atop the ARC layer. The Ti disks were used as a selective mask while etching through the ARC layer using O₂ reactive ion etching, followed by three consecutive e-beam evaporations to deposit Au (30 nm), Al₂O₃ (60 nm) and Au (30 nm). Finally, an O₂ plasma ash was used to remove the ARC posts and form the final structures as shown in Fig. 2.

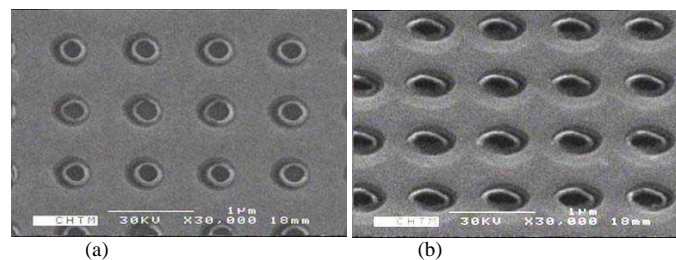


Fig. 2. Scanning electron microscopy (SEM) pictures of Au-Al₂O₃-Au samples with (a) circular and (b) elliptical holes.

A somewhat different process was used to fabricate the rectangular holes through the multilayer. First, we used a single exposure to make a 1D pattern in the PR on BARC layer, followed by development, etching through the BARC layer using the 1D PR pattern as the selective etching mask, and selective removal of the PR with acetone. A second PR layer was spun onto the 1D BARC pattern, exposed at right angles to the original 1D pattern, etched through the 1D BARC pattern using the PR pattern as an etching mask and then removed,

leaving a 2D array of rectangular BARC posts as shown in Fig. 3. As described above, the three layers, Au/Al₂O₃/Au, were deposited by e-beam evaporation. As the final step of fabricating the rectangular holes through the gold and aluminum-oxide films, a fully isotropic, high pressure O₂ plasma ash was carried out to remove the BARC posts leading to the final structure (528 nm, 339 nm on long and short sides, respectively) as shown in Fig. 4, which also shows the advantage of large area of patterning using IL techniques [18].

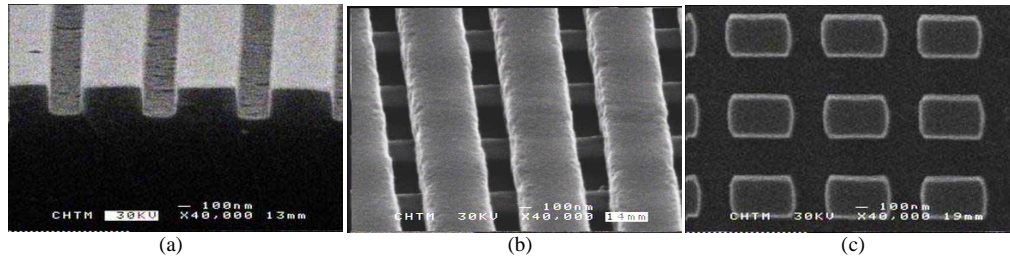


Fig. 3. SEM pictures of samples: (a) 1D PR pattern on ARC layer (b) 1D PR pattern perpendicular to 1D ARC pattern (c) ARC post (top view)

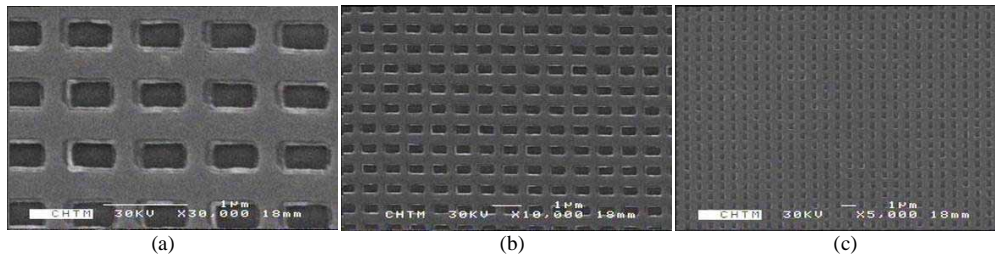


Fig. 4. SEM pictures of completed fishnet structure samples.

3. Measurement and simulation

The transmission of these samples across the near-infrared wavelength region ($\sim 2 \mu\text{m}$) was measured at normal incidence using Fourier-transform infrared spectroscopy (FTIR). The measured transmission spectra were normalized to the spectrum of a bare BK7 glass standard. In the case of the symmetric NIM with circular holes, an unpolarized FTIR beam was used to measure the transmission. For the asymmetric structures (NIMs with elliptical and rectangular holes), the incident electric field was either parallel to the narrower stripe width between apertures (E_{par}), or parallel to the wider stripe width between apertures and perpendicular to the narrow direction (E_{per}). The transmission spectra of samples with circular, elliptical and rectangular holes for both E_{per} and E_{par} are shown in Figs. 5(a)-5(c).

A rigorous coupled wave analysis (RCWA) simulation, a commonly used algorithm to compute the spectra of transmission and reflectance of periodic structures [19,20], was used to calculate the transmission spectra to understand properties of these different structures such as effective refractive index, the figure of merit (FOM), impedance, effective permittivity (permeability) and so on. The present version of the simulation software is restricted to rectangular holes. Therefore, for the circular case, the aperture was modeled as a square with the same open area as the circle. For the elliptical case, a rectangular geometry was calculated with open area and the ratio of side length the same as the area and the major/minor axis ratio of the ellipse. Metal/dielectric/metal thicknesses of 30/60/30 nm were used in the simulation. This code was used to analyze the initial circular aperture NIM and a detailed comparison of experiment and simulation for amplitude and phase of transmission and reflection was presented [13]. Zhang and Dolling have both measured the amplitude and phase of reflection and transmission and demonstrated that this modeling procedure gives a good fit to the

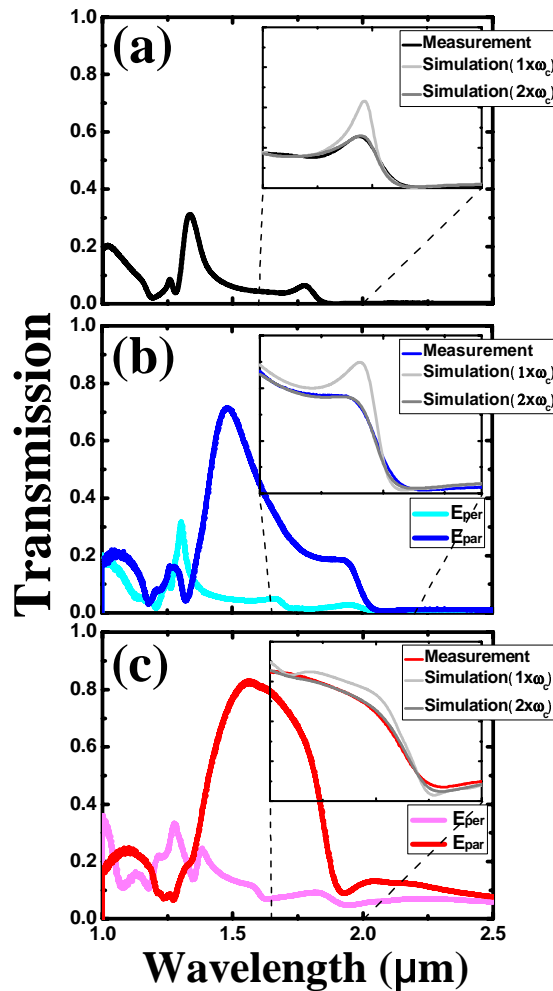


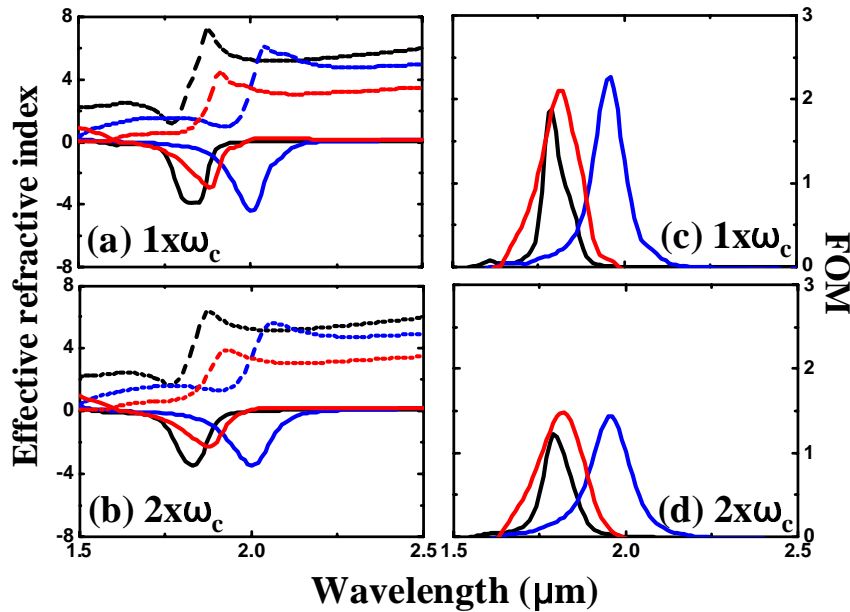
Fig. 5. Measured normal incidence transmission spectra for E_{par} and E_{per} polarization using FTIR. NIMs with (a) circular (b) elliptical (c) rectangular holes. Insets show a comparison of E_{par} transmission spectra calculated by RCWA model and measurement across the negative refractive index region with one ($1 \times \omega_c$) and two times ($2 \times \omega_c$) the bulk scattering frequency in a Drude model for the metal permittivity.

experimentally measured index and impedance (or permittivity and permeability); those measurements are not repeated here [13,17].

A simple Drude model for the metal permittivity was used, which is a good approximation to experiment values in the near-IR. The permittivity is given as $\epsilon_{Au} = 1 - \omega_p^2 / [\omega(\omega + i\gamma\omega_c)]$, where ω_p (plasma frequency) = 1.37×10^{16} Hz and ω_c (bulk scattering frequency) = 4.1×10^{13} Hz [21]. γ is a fitting parameter to account for additional scattering in the thin, multi-domain films as well as for any sample inhomogeneity across the ~ 1 cm² measurement area [13]. [Spectra measured on small areas across the sample show very good uniformity with only small variations in spectra, much less than the observed structural variations]. Insets of Fig. 5 show that the structure (dips and peaks) in the region of negative refractive index becomes less distinct as γ is increased. Two times the scattering frequency ($\gamma = 2$) of bulk gold was found to give the best fit between experiment and simulation over the range of wavelengths of interest for all three structures as shown in the insets to Fig. 5. This allows us to extract the

effective refractive index, impedance, permittivity and permeability over the range of negative refraction from simulation. The effective refractive index and impedance were extracted from the complex coefficients of transmission and reflection obtained by a RCWA simulation as shown in Figs. 6(a), 6(b) and Figs. 7(a), 7(b) [5, 22]. The effective refractive indices (n_{eff}) of NIMs with circular, elliptical and rectangular holes are shown in Figs. 6(a), 6(b). For the three different NIM structures, a negative refractive index is obtained over a range of wavelengths (1.56 μm to 2 μm , 1.64 μm to 2.2 μm and 1.64 μm to 1.98 μm for NIMs with circles, ellipses and rectangles, respectively). For a smaller scattering frequency ($\gamma = 1$), larger real parts and smaller imaginary parts of effective refractive index are obtained as shown in Fig. 6(a). For simulation with $\gamma = 2$, the minimum real parts of effective refractive index ($-\text{Re}[n_{eff}]$) are larger than the imaginary parts of the index ($\text{Im}[n_{eff}]$) as shown in Fig. 6(b), e. g. $\text{FOM} > 1$ which is improved compared with previous reports [13,16]. The FOM is plotted in Figs. 6(c), 6(d). For thin metal lines along the electric field, E_{par} polarization, electric field along the narrow stripes, the FOMs using $\gamma = 2$ are 1.22, 1.43 and 1.48 for NIM with circular, elliptical and rectangular holes, respectively. In Fig. 6(d), the circular structure has a somewhat smaller FOM, however the results for the elliptical and fishnet structures are quite similar. These FOMs for circular and elliptical structures are higher than the results in Refs. [13, 16], suggesting that the present samples have an improved homogeneity. For reference, peaks of FOMs using $\gamma = 1$ are approximately 1.88, 2.26 and 2.11 in Fig. 6(c). As a result of uncertainty in the modeling (particularly the use of a rectangular structure to model all three experimental samples), these results should be interpreted only qualitatively to suggest that there is not a strong structural dependence of the FOM.

Over the wavelength range of negative refraction, the effective impedance (ζ_{eff}) for each structure is shown in Fig. 7, the real part of the impedance for the fishnet structure is closer to the $\sqrt{\zeta_{air}\zeta_{glass}} \sim 1.2$ required for antireflection coating the glass-air interface, which indicates that NIM with rectangular holes $>$ elliptical holes $>$ circular holes is the order of both higher transmission and better impedance matching between the NIM and the superstrate ($\zeta_{air} = 1$),



Figs. 6. (a). and 6(b). Real (solid lines) and imaginary (dashed lines) parts of the effective refractive index using the scattering frequencies one ($1 \times \omega_c$) and two times ($2 \times \omega_c$) that of bulk gold, respectively. 6(c), 6(d) FOMs using $1 \times \omega_c$ and $2 \times \omega_c$. The same color convention as Fig. 5 is followed (black: NIM with circular holes, blue: NIM with elliptical holes and red: NIM with rectangular holes)

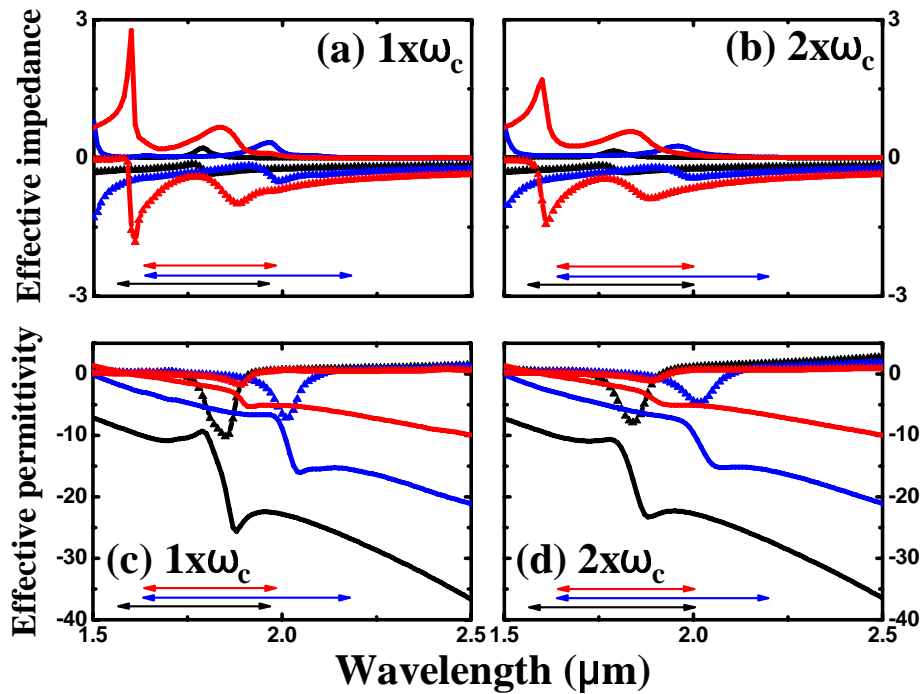


Fig. 7. (a), 7(b). The calculated effective impedance (ζ_{eff}). 7(c), 7(d) effective permittivity (ϵ_{eff}). Real parts of ζ_{eff} and ϵ_{eff} are indicated by solid lines and imaginary parts are plotted with symbols. The same color convention as Fig. 5 is followed. Arrows represent the negative refractive index region of NIM with circles, ellipses and rectangles, respectively.

substrate ($\xi_{glass} = 1.5$) combination. In Fig. 5(c), the transmission in the region of negative index is as high as ~80% with rectangular holes, which is improved in comparison with the low transmission obtained in NIM with circles and ellipses due to better impedance matching as shown in Figs. 7(a), 7(b). The calculated effective permittivity (ϵ_{eff}) and permeability (μ_{eff}), shown in Figs. 7(c), 7(d) and Fig. 8, can be extracted from the effective refractive index (n_{eff}) and impedance (ζ_{eff}) by simple calculation ($\mu_{eff} = n_{eff} \times \zeta_{eff}$ and $\epsilon_{eff} = n_{eff} / \zeta_{eff}$). The effective permittivity, Figs. 7(c), 7(d) resembles the permittivity of a dilute Drude metal, in addition, the real parts of the effective permeability show a resonant modulation around 1.8 μm (for circular and rectangular holes) and 2 μm (for elliptical holes) and the imaginary parts show peaks, reflecting the magnetic resonance behavior. $\text{Re}[\mu_{eff}]$ has negative values for all three structures for $\gamma = 1$ whereas for $\gamma = 2$ the minimum value of $\text{Re}[\mu_{eff}]$ of NIM with circular holes is not negative; it is negative for the elliptical and rectangular structures. [In Ref. [13], only results for $\gamma = 3$ were presented and a negative $\text{Re}[\mu_{eff}]$ was not achieved]. Figures 7(c), 7(d) and Fig. 8 indicate that the influence of the scattering frequency (γ) is predominantly on the effective permeability (μ_{eff}) as expected.

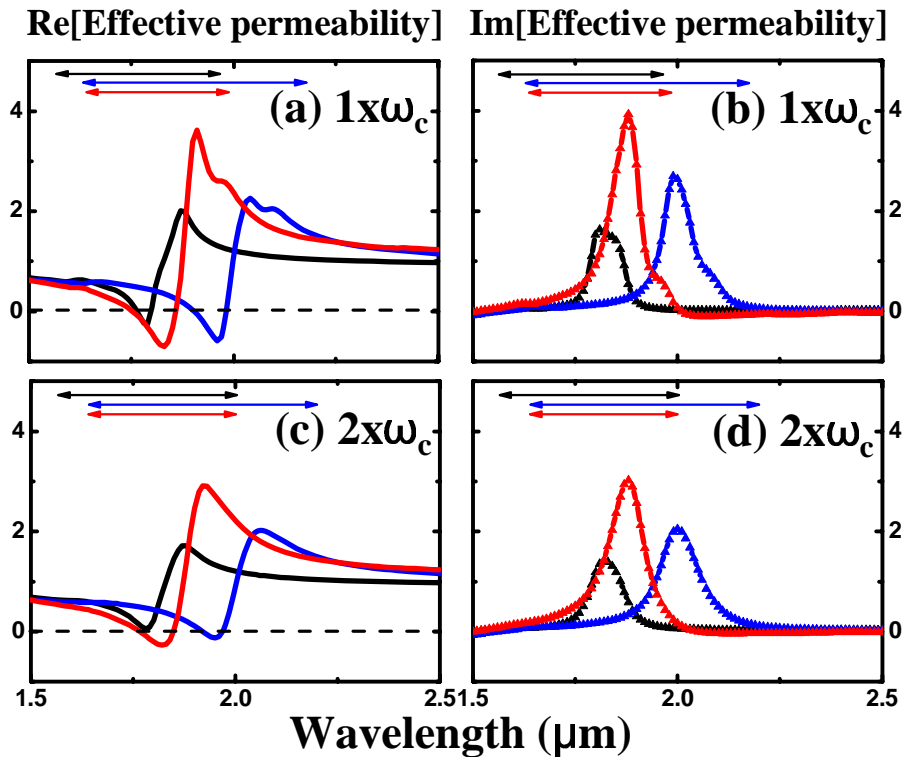


Fig. 8. (a) – 8(d) The effective permeability (μ_{eff}). The color convention is the same as in Fig. 5.

4. Summary

In conclusion, the impact of the geometry (circular, elliptical and rectangular apertures) and of metal electron scattering rates on the optical properties of negative-index materials has been examined. The experimental results are in good agreement with a RCWA simulation and with the progression of improved impedance matching in moving from circular to elliptical to rectangular apertures. A transmission of over 80% was achieved in the negative index region for the rectangular aperture geometry. The FOMs are very similar for all three geometries with NIMs with ellipses and rectangular structures being about 20% higher than for circular structures. The simulations were restricted to rectangular structures, and while excellent agreement was achieved with measured transmission spectra, additional simulations that fully take into account the impacts of the actual non-rectangular aperture geometries are needed to confirm the effects of structure on the FOM.

Acknowledgments

This work was supported by DARPA under the University Photonics Research Center program. We are grateful to S. Zhang for providing us with the RCWA code and for technical discussions. Facilities of the NSF-sponsored NNIN node at the University of New Mexico were used for the fabrication.